

Coherent Association of Single Molecules from Single Atoms

A DISSERTATION PRESENTED
BY
YICHAO YU
TO
THE DEPARTMENT OF PHYSICS

IN PARTIAL FULFILLMENT OF THE REQUIREMENTS
FOR THE DEGREE OF
DOCTOR OF PHILOSOPHY
IN THE SUBJECT OF
PHYSICS

HARVARD UNIVERSITY
CAMBRIDGE, MASSACHUSETTS
MARCH 2021

©2021 – YICHAO YU
ALL RIGHTS RESERVED.

Thesis advisor: Professor Kang-Kuen Ni

Yichao Yu

Coherent Association of Single Molecules from Single Atoms

ABSTRACT

Contents

o	INTRODUCTION	1
1	APPARATUS	2
1.1	Laser Sources	2
1.2	Cooling Beams	2
1.3	Tweezer and Imaging	3
1.4	Molecular Raman Frequency Generation	3
2	COMPUTER CONTROL OF THE EXPERIMENT	4
2.1	Overall Structure	4
2.2	Frontend	4
2.3	Backends	5
2.4	Automation of Scan	5
2.5	Summary and Outlook	5
3	RAMAN SIDEBAND COOLING	6
3.1	Introduction	6
3.2	Basic Theory	8
3.3	Raman Sideband Thermometry	12
3.4	Setup	13
3.5	Cooling Performance and Challenge with Large Lamb-Dicke Parameter	15
3.6	Solution: High Order Sidebands	17
3.7	Solution: Simulation Based Optimization	19
3.8	Alignment of Raman and OP Beams	20
3.9	Calibration	20
3.10	Cooling Performance	20
4	INTERACTION OF SINGLE ATOMS	24
4.1	Scattering Length	24
4.2	Energy Levels of Two Interacting Atoms in an Anisotropic Trap	24
4.3	Interaction Shift Spectroscopy	25
4.4	Summary and Outlook	25
5	PHOTOASSOCIATION OF SINGLE ATOMS	26
5.1	Energy Levels	26

5.2	Effect of the Trap	26
5.3	Photoassociation Spectroscopy	27
6	TWO-PHOTON SPECTROSCOPY OF NaCs GROUND STATE	28
6.1	Introduction	29
6.2	Energy Level Structure for NaCs Ground State	29
6.3	Raman Resonance on $v'' = -1$, $N = 0$ Ground State	29
6.4	Raman Resonance on $v'' = -1$, $N = 2$ Ground State	29
7	COHERENT OPTICAL CREATION OF NaCs MOLECULE	30
7.1	Introduction	31
7.2	Raman Transition Beyond Three-Level Model	31
7.3	Raman Transfer versus STIRAP	38
7.4	States Selection	40
7.5	Raman Transfer Results	40
8	CONCLUSION	41
	APPENDIX A COMPUTER CONTROL HARDWARE SPECIFICATION	42
	APPENDIX B FULL RAMAN SIDEBAND COOLING SEQUENCE	43
	REFERENCES	50

Acknowledgments

,

0

Introduction

1

Apparatus

1.1 LASER SOURCES

1.2 COOLING BEAMS

(MOT, OP, Raman)

1.3 TWEEZER AND IMAGING

1.4 MOLECULAR RAMAN FREQUENCY GENERATION

(Maybe moved to later chapter) (beam path, calibration)

2

Computer Control of the Experiment

2.1 OVERALL STRUCTURE

2.2 FRONTEND

(Abstraction) (Backward compatibility) (Flexibility) (Text based/version control friendly)

2.3 BACKENDS

(communication protocol) (IR)

2.3.1 FPGA BACKEND

(clock generation) (pulse merging) (compression)

2.3.2 NIDAQ BACKEND

(Variable clock)

2.3.3 USRP BACKEND

(SIMD)

2.4 AUTOMATION OF SCAN

(Scan requirement) (Combination of scans) (Scope/nested structure)

2.5 SUMMARY AND OUTLOOK

(new backend/SPCM) (native code generation, auto vectorization) (dynamic logic and dependency tracking/optimization)

3

Raman Sideband Cooling

3.1 INTRODUCTION

(In order to achieve full quantum control on molecules, we need to control atoms first.) (An example of such control) (Motional degrees of freedom) (PGC cools to ...) (RSC to further cool.)



Figure 3.1: Single Na atom Raman sideband cooling scheme. The Raman transitions couples $|2, 2; n\rangle$ and $|1, 1; n + \Delta n\rangle$ through the intermediate states $|e_i\rangle$ in the $3^2P_{3/2}$ electronic states. The transitions have a one-photon detuning $\Delta_i \approx 75$ GHz. Two-photon detuning, δ , is defined relative to the $\Delta n = 0$ carrier transition. For optical pumping, we use two σ^+ polarized transitions, one to pump the atom state out of $|1, 1\rangle$ via $3^2P_{3/2}$ and one to pump atoms out of $|2, 1\rangle$ via $3^2P_{1/2}$ to minimize heating of the $|2, 2\rangle$ state.

3.2 BASIC THEORY

The relevant energy diagram and the laser frequencies for RSC are shown in Fig. 3.1. We approximate the trapping potential using a harmonic oscillator. Since this is a separable potential, we can use only the 1D motional state $|n\rangle$ and the result can be easily generalized to the full 3D system.

The cooling sequence consists of two types of pulses. First, a Raman pulse drives the atom to a different hyperfine state while simultaneously reduces the motional energy of the atom. The optical pumping (OP) pulse afterwards then reset the hyperfine state of the atom and reduce the entropy of the system. This sequence is then repeated until the system reaches the ground motional state where there is no more motional energy to be taken out of the system via the Raman pulse. In this section, we will discuss the theory of each types of pulses individually. We will cover how the pulses affect cooling performance in section 3.5.

3.2.1 RAMAN TRANSITION

As shown in Fig. 3.1, the cooling sequence starts with the sodium atom in the $|s_1\rangle \equiv |2, 2\rangle$ hyperfine state, and a Raman transition is used to drive the atom to the $|s_2\rangle \equiv |1, 1\rangle$ state, where $|F, m_F\rangle$ denotes the F and m_F quantum number for the sodium atom. The full Rabi frequency for such a transition is given by

$$\Omega_R^0 = \sum_i \frac{\Omega_{1i}\Omega_{2i}^*}{2\Delta_i} \quad (3.1)$$

where the sum is over all the coupled excited states, $\Omega_{ai} \equiv \langle a | \mathbf{d} \cdot \mathbf{E}_a | e_i \rangle$ is the single photon Rabi frequency between $|a\rangle$ and $|e_i\rangle$ and Δ_i is the single photon detuning from excited state $|e_i\rangle$.

In order to account for the motional degrees of freedom, we need to include the spatial wavefunction of the atom and light into account. As mentioned above, we approximate the atomic motional wavefunction by the harmonic oscillator eigenstates $|n\rangle$. Coupling between states different n states from the Raman transition is allowed due to the recoil from the Raman lasers, which corresponds to a spacial phase imprinting of $e^{i\Delta\mathbf{k} \cdot \mathbf{x}}$ where $\Delta\mathbf{k}$ is the wavevector difference between the two Raman beams. Using the creation (\hat{a}^\dagger) and annihilation (\hat{a}) operators and the relation $\mathbf{x} = x_0(\hat{a} + \hat{a}^\dagger)$ where $x_0 = \sqrt{\hbar/2m\omega}$ is the harmonic oscillator length, the phase factor can be expressed as $e^{i\eta^R(\hat{a} + \hat{a}^\dagger)}$ where $\eta^R \equiv \Delta\mathbf{k} \cdot \mathbf{x}_0$ is the Lamb-Dicke parameter for the Raman transition. The matrix element between motional state $|n\rangle$ and $|n'\rangle$ is therefore,

$$M_{n,n'} = \langle n | e^{i\eta^R(\hat{a} + \hat{a}^\dagger)} | n' \rangle$$

and the final Raman Rabi frequency between motional states n and n' is given by,

$$\Omega_R^{n,n'} = M_{n,n'} \Omega_R^0$$

For $n = n'$, this is called a carrier transition and the others are called sideband transitions. If the final state is higher than the initial one, i.e. $n' > n$, it is a heating sideband. Likewise, transitions with $n' < n$ are cooling sidebands.

A closed form result for $\mathcal{M}_{n,n'}$ is given in ,

$$\mathcal{M}_{n,n'} = e^{(\eta^R)^2/2} \sqrt{\frac{n_{<}!}{n_{>}!}} (\eta^R)^{|n-n'|} L_{n_{<}}^{|n-n'|} \left((\eta^R)^2 \right)$$

where $n_{<}$ and $n_{>}$ are the lesser and greater, respectively, of n and n' , and L_n^α is the generalized Laguerre polynomial,

$$L_n^\alpha(x) \equiv \sum_{m=0}^n (-1)^m \binom{n+\alpha}{n-m} \frac{x^m}{m!}$$

An important limit is the so-called Lamb-Dicke (LD) regime defined by $(\eta^R)^2(2n+1) \ll 1$. In this case, we can approximate the phase factor in leading order of η^R ,

$$e^{i\eta^R(\hat{a}+\hat{a}^\dagger)} \approx 1 + i\eta^R(\hat{a} + \hat{a}^\dagger)$$

and the matrix element

$$\mathcal{M}_{n,n'} \approx \delta_{n,n'} + i\eta^R \sqrt{n+1} \delta_{n+1,n'} + i\eta^R \sqrt{n} \delta_{n,n'+1}$$

the three terms corresponds to the carrier ($n' = n$), the first order heating sideband ($n' = n+1$) and the first order cooling sideband ($n' = n-1$) with corresponding strength 1 , $\eta^R \sqrt{n+1}$ and $\eta^R \sqrt{n}$. We can clearly see from this approximation that the coupling to other motional state is stronger for a larger η^R and higher motional quantum number n . We will discuss this effect outside the LD regime and its implication on the cooling performance in more detail in section 3.5.

SCATTERING FROM RAMAN BEAMS

In addition to driving the Raman transition, the Raman beams can also cause scattering. The rate of the scattering is *,

$$\Gamma = \sum_i \frac{\Gamma_{ei} \Omega_{li}^2}{4\Delta_i^2}$$

where Γ_{ei} is the linewidth of the excited state $|e_i\rangle$. Together with (3.1), we see that approximately $\Gamma/\Omega_R \propto 1/\Delta$ so a larger detuning should be used in order to reduce the scattering during RSC.

3.2.2 OPTICAL PUMPING

Driving the system on a cooling sideband with Raman transition can reduce the motional energy of the atom. However, this is a fully coherent process that does not reduce the system entropy and is not really “cooling” the system or achieving better control on the quantum state of the system. Instead, quantum state control is achieved in the RSC via the OP pulse. The initial hyperfine state $|2, 2\rangle$ is a stretched state so it is the state the system naturally ends up in when σ^+ light is applied. However, if this is done using scattering from a $F = 2$ to $F' = 3$ transition, the OP beam will allow continuous photon cycle between the $|2, 2\rangle$ and the $|3', 3\rangle$ causing unnecessary motional heating during OP. Therefore, the OP must be done on a $F = 2$ to $F' = 2$ transition. Unfortunately, for Na, the corresponding transition from $3^2S_{1/2}$ to $3^2P_{3/2}$ that is used for the MOT is not useable due to

*Here we assume that each Raman beam only couples to their respective ground states. Including coupling to the other ground state increases the scattering rate but does not change the scaling with detuning.

the small energy difference of 60MHz (or 6 line widths) between the $F = 2$ and $F = 3$ states ^{Steck}.

Instead, we must use the sodium D1 line, i.e. $3^2S_{1/2}$ to $3^2P_{1/2}$ transition, which lacks a $F = 3$ excited state. The D1 light with σ^+ polarization is only used to pump atoms from $F = 2$ states (in particular $|2, 1\rangle$ which is populated during the OP process). Since the goal of the OP pulse is to clear the atom population in all states but $|2, 2\rangle$, the photon cycling is not a concern for $F = 1$ states and the D2 line is used for OP of $F = 1$ states instead. This also allow us to reuse the MOT light source and simplifies our setup.

3.3 RAMAN SIDEBAND THERMOMETRY

From the discussion in section 3.2.1, we see that the strength of the sideband transition depends on the initial motional state as well as the Lamb-Dicke parameter η^R of the atom. This dependency allows us to infer the motional state of the atom by measuring the sideband height, i.e. the so-called sideband thermometry.

In particular, for atom with temperature T , the probability for the atom to be in motional state $|n\rangle$ is,

$$p_n = \frac{e^{-n\hbar\omega/k_B T}}{1 - e^{-\hbar\omega/k_B T}}$$

for a Raman pulse with full Rabi frequency Ω_R^0 and time t , the peak height for the first order heating (+) and cooling (-) sidebands,

$$h_{\pm} = \sum_{n=0}^{\infty} p_n \sin^2 \left(\frac{\Omega_R^0 t}{2} M_{n,n\pm 1} \right)$$

note that $p_{n+1} = p_n e^{-\hbar\omega/k_B T}$, $M_{n,n'} = M_{n',n}$ and $M_{n,-1} = 0$, we have

$$\begin{aligned}
h_- &= \sum_{n=0}^{\infty} p_n \sin^2 \left(\frac{\Omega_R^0 t}{2} M_{n,n-1} \right) \\
&= e^{-\hbar\omega/k_B T} \sum_{n=1}^{\infty} p_{n-1} \sin^2 \left(\frac{\Omega_R^0 t}{2} M_{n-1,n} \right) \\
&= e^{-\hbar\omega/k_B T} h_+
\end{aligned}$$

Therefore, if we measure the ratio of the cooling and heating sideband heights $\alpha \equiv h_-/h_+$, we can calculate the temperature of the atom with $e^{-\hbar\omega/k_B T} = \alpha$. The corresponding ground state probability is,

$$\begin{aligned}
p_0 &= \frac{1}{1 - e^{-\hbar\omega/k_B T}} \\
&= \frac{1}{1 - \alpha}
\end{aligned}$$

We will use this to experimentally characterize the performance of the cooling sequence in the following sections.

3.4 SETUP

The geometry of all the beams and field involved is shown in Fig. 3.2. In order to make the cooling more efficient and simplify the sideband thermometry, we address the motion along the three principle axis of the tweezer using different pairs of Raman beams. In order to maximize the beam



Figure 3.2: Geometry and polarizations of the Raman and optical pumping beams relative to the optical tweezer and bias magnetic field. Raman beams R1 and R4 address the radial x -mode. R1 and R2 address the radial y -mode. R3 and R4 address the axial z -mode, where the beams also couple to radial motion, but this coupling can be neglected when the atoms is cooled to the ground state of motion.

intensity so that a larger single photon detuning can be used while maintaining the same Raman Rabi frequency, we focus the Raman beam onto the single atom with a waist of $\approx 100\mu\text{m}$. The maximum powers within each Raman beam are between 1 and 6mW which give us a maximum Raman Rabi frequency of 50 to 200kHz.

We apply an external bias magnetic field of 8.8G parallel to the polarization of the tweezer beam (and orthogonal to the tweezer beam propagation direction). This makes the field orthogonal to the effective magnetic field of the tweezer, which minimizes the vector light shifts [Kaufman et al., Thompson et al.](#). Since the optical pumping beam requires σ^+ polarization, it is setup to propagate parallel to the applied magnetic field.

3.5 COOLING PERFORMANCE AND CHALLENGE WITH LARGE LAMB-DICKE PARAMETER

RSC is typically performed in the LD regime where the coupling to other motional state is small.

Due to the light mass, short wavelength, limited trap depth and high initial temperature of the sodium atom however, we have to start our RSC sequence outside the LD regime. This creates unique challenges to our experiment. A detailed understanding of the cooling performance is required to understand and overcome these challenges.

The simplest way to estimate the effectiveness of RSC is by keeping track of the average energy of the atom during the cooling sequence. For a typical RSC sequence in the LD regime, all the cooling are done on the strongest first order cooling sideband. The energy removed for atom driven in one Raman pulse is therefore, $\Delta E_- = \omega$. In order to reinitialize the hyperfine state, the sodium atom needs to scatter on average 2 photons from the OP pulse which increases the average energy of the driven atom by $\Delta E_+ = 4\omega_r$ [†] where $\omega_r \equiv \hbar k^2/2m$ is the recoil energy^{Steck} and k is the OP light wave vector. The heating to cooling ratio in one RSC pulse cycle is therefore,

$$\begin{aligned}\frac{\Delta E_+}{\Delta E_-} &= \frac{2\hbar k^2}{m\omega} = 4k^2 x_0^2 \\ &= 4(\eta^{OP})^2\end{aligned}$$

where $\eta^{OP} \equiv kx_0$ is the Lamb-Dicke parameter for OP. Therefore, in order to achieve net cooling, we need $(\eta^{OP})^2 < 0.25$. In 3D with cooling along multiple axis with different trapping frequency

[†]The factor of 4 comes from 2 absorbed photons and 2 reemitted photons.



Figure 3.3: Optical pumping motional-state redistribution and Raman coupling for large LD parameters for the axial direction (z). The range plotted covers 95% of the initial thermal distribution. (A) Motional state distribution after one OP cycle for different initial states motion, n_{init} . Due to photon-recoil and the large LD parameter, $\eta_z^{OP} = 0.55$, there is a high probability of n changing. (B) Matrix elements for Raman transition on the first order cooling sideband deviate from \sqrt{n} scaling with multiple minima.

(and therefore different η^{OP}), the $(\eta^{OP})^2$ in the requirement is replaced by a weighted average of different axis depending on the frequency each axis is cooled in the sequence.

In our experiment, the OP Lamb-Dicke parameters are $\eta_x^{OP}, \eta_y^{OP}, \eta_z^{OP} = 0.25, 0.25, 0.55$. Based on the metric above, any cooling sequences that have fewer than 78% cooling pulse for z (axial) axis, which is generally the case, should have a net cooling effect. This, however, does not guarantee cooling into the ground motional state, nor does it fully characterize the efficiency of the cooling sequence since the averaging hides a few critical aspect of having a large Lamb-Dicke parameter.

One of the important effects can be seen in Fig. 3.3A showing the motional state distribution after one OP cycle for different initial motional states n_{init} . Although the average heating is fixed at $4\omega_r$, independent of n_{init} , the spread or the uncertainty of n after the OP is significantly higher for high n_{init} . This effect significantly increases the difficulty in controlling the state during the RSC sequence. It can negatively impact the cooling performance and may lead to increased loss during

cooling due to atom escaping to higher motional states.

The other important effect is the dependency of matrix element $\mathcal{M}_{n,n+1}$ on the motional level n . While this dependency is not a new effect, since the \sqrt{n} dependency on the cooling sideband strength exist even in the LD regime and must be taken into account with pulse time variation to achieve efficient cooling, the high Lamb-Dicke parameter adds even more complications. As shown in Fig. 3.3B, rather than a simple \sqrt{n} dependency, it is a non-monotonic function and more importantly has multiple minima, so-called “dead-zone”, within the range of motional states we are interested in. The coupling strength for states in the dead-zones can be reduced by more than ten times which can significant affect the efficiency of the cooling pulse and even makes it virtually impossible to drive Raman transitions on atoms in these states in order to cool them further. A cooling sequence can therefore accumulate pupolations in the dead-zones rather than the ground state. Their small coupling strength also reduce their signal level during Raman sideband spectroscopy making these states nearly invisible to sideband thermometry which further complicates the optimization of the cooling sequence.

3.6 SOLUTION: HIGH ORDER SIDEBANDS

The main solution to the issues related to the large Lamb-Dicke parameter is in fact the large Lamb-Dicke parameter itself. The increased coupling to other motional state for large Lamb-Dicke parameter and high motional states applies not only to $|\Delta n| = 1$ but to higher Δn as well. Fig. 3.4 shows the coupling to higher order cooling sidebands which all have comparable strengths as the first order



Figure 3.4: Matrix elements for Raman transition including high order sidebands. During cooling, we utilize the fact that high motional states couple most effectively to sidebands with large $|\Delta n|$ in order to overcome the issue with variation and dead zone in the coupling strengths.

sidebands in different ranges of motional states.

Because of this, it is now possible, and in some cases preferred, to apply Raman cooling pulse on the higher order sidebands instead of only the first order one. These pulses reduce more energy from the system per pulse which directly improves the cooling to heating ratio and allows better control on the motional state given the uncertainty after an OP pulse. More importantly, depending on the motional level, there is always a sideband order with significant coupling strength that can be used to cool it, therefore completely removing the coupling dead-zones. Moreover, by using each sideband orders only near their coupling maxima, the coupling strength variation is also greatly reduced which removes the need to vary the pulse times for all but the pulses on the first order sideband.

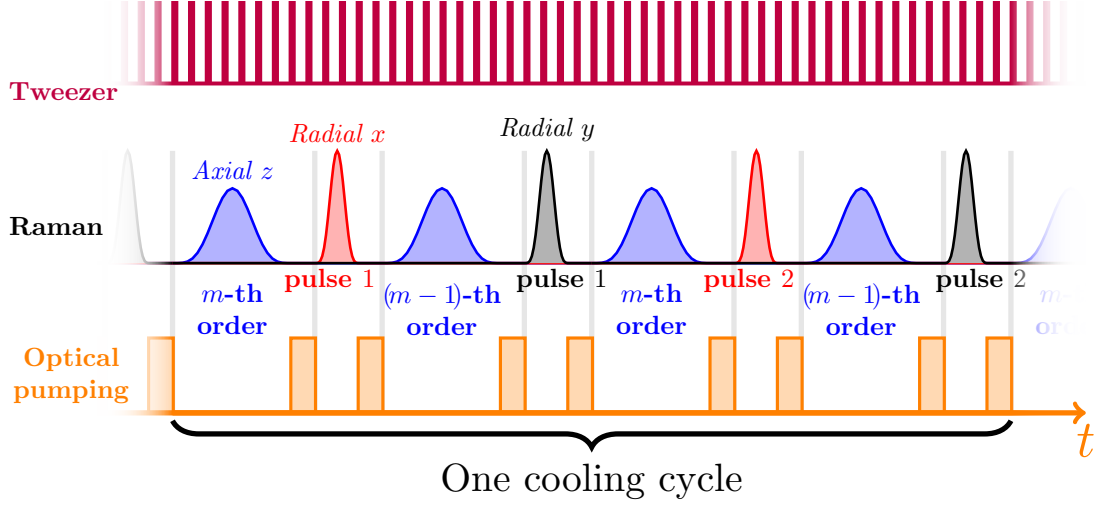


Figure 3.5: Schematic of the cooling pulse sequence. The tweezer is strobed at 3 MHz to reduce light shifts during optical pumping ^{Hutzler et al.}. Each cooling cycle consists of 8 sideband pulses. The four axial pulses address two sideband orders. The two pulses in each radial direction either address $\Delta n = -2$ and $\Delta n = -1$ or have different durations to drive $\Delta n = -1$, at the end of the cooling sequence when most of the population is below $n = 3$. The Raman cooling and spectroscopy pulses have Blackman envelopes ^{Kasevich & Chu} to reduce off-resonant coupling, while the measurement Rabi pulses in Fig. 3.7 have square envelopes to simplify analysis.

3.7 SOLUTION: SIMULATION BASED OPTIMIZATION

The change in cooling technique by including higher order sidebands, however, does not remove the effect of coupling variation on the sideband thermometry. If a non-thermal distribution of motional states is produced by the cooling sequence, the ratio of the first order sideband height still cannot be trusted to calculate the temperature or the ground state probability. Including higher order sidebands in the sideband thermometry could in principle give us enough information about the state distribution but doing so for a non-thermal distribution is not easy or reliable. We therefore use a Monte-Carlo simulation to guide our search for the optimal sequence. Fig. 3.5 demonstrate the sequence from the simulation. In particular, we find that alternating the cooling pulses between two

neighboring orders for the axial direction and $\Delta n = -2$ and $\Delta n = -1$ for the radial directions eliminates the accumulation of population in motional states with small Raman coupling. The simulation also confirms that setting the coupling strength of each sideband to drive a Rabi π -pulse corresponding to the maximum matrix element motional state (i.e. the maxima in Fig. 3.4) yields efficient cooling, initially, as we expected from section 3.6. The efficiency of cooling on higher-order sidebands diminishes as the atom approaches the ground state, so the final cycles utilize only the $\Delta n = -1$ sideband while alternating between the three axes.

3.8 ALIGNMENT OF RAMAN AND OP BEAMS

(Back reflection of OP)

3.9 CALIBRATION

(Sideband/carrier) (Cold vs hot)

3.10 COOLING PERFORMANCE

3.6 3.7

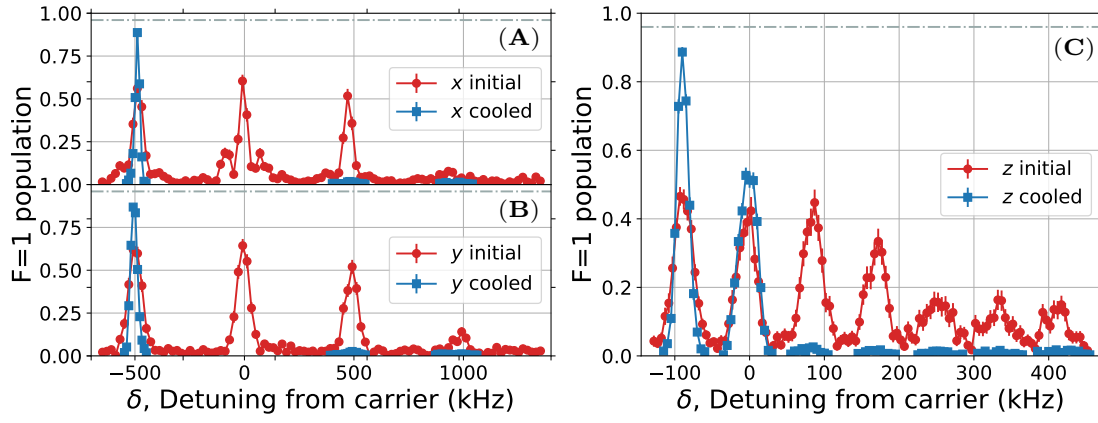


Figure 3.6: Raman sideband spectra for (A) x , (B) y , (C) z axis before (red circle) and after (blue square) applying Raman sideband cooling sequence. The height of the cooling sidebands (positive detuning) are strongly suppressed after cooling which suggests most of the atoms are cooled to the motional ground state in the trap.

Figure 3.7 (following page): Rabi flopping on radial axis x (A) carrier and (B) $\Delta n_x = 1$ sideband, radial axis y (C) carrier and (D) $\Delta n_x = 1$ sideband, axial axis z (E) carrier and (F) $\Delta n_x = 1$ sideband, before (red circle) and after (blue square) Raman sideband cooling.

Solid lines (both red and blue) in all plots are fits to a Rabi-flopping that includes a thermal distribution of motional states [Meekhof et al.](#) as well as off-resonant scattering from the Raman beams.

The blue lines correspond to a ground state probability of (A-D) 98.1% along radial axis and (E-F) 95% along the axial axis after cooling. The red lines correspond to a thermal distribution of 80 μ K before RSC. The horizontal dashed lines in all the plots correspond to the 4 % probability of imaging loss.

The green dashed line in (F) includes the additional decoherence due to a fluctuation of the hyperfine splitting of magnitude 3 kHz. We see that the decoherence effect is strongest for the post-cooling data on the axial $\Delta n_z = 1$ sideband where the Rabi frequency is the lowest.

Figure 3.7: (continued)



4

Interaction of Single Atoms

4.1 SCATTERING LENGTH

(Importance/relation with binding energy etc.)

4.2 ENERGY LEVELS OF TWO INTERACTING ATOMS IN AN ANISOTROPIC TRAP

(appendix?)

4.3 INTERACTION SHIFT SPECTROSCOPY

(motional sideband, scattering length result)

4.4 SUMMARY AND OUTLOOK

(Motional state selection)

5

Photoassociation of Single Atoms

5.1 ENERGY LEVELS

5.2 EFFECT OF THE TRAP

(light shift, broadening)

5.3 PHOTOASSOCIATION SPECTROSCOPY

($v=0, 12, 14$, etc)

6

Two-photon Spectroscopy of NaCs

Ground State

6.1 INTRODUCTION

6.2 ENERGY LEVEL STRUCTURE FOR NaCs GROUND STATE

6.3 RAMAN RESONANCE ON $v'' = -1$, $N = 0$ GROUND STATE

6.4 RAMAN RESONANCE ON $v'' = -1$, $N = 2$ GROUND STATE

7

Coherent Optical Creation of NaCs

Molecule

7.1 INTRODUCTION

7.2 RAMAN TRANSITION BEYOND THREE-LEVEL MODEL

In an ideal three-level system, the scattering probability during a π pulse Raman transition can be made arbitrarily small by using a large single photon detuning^(3.2.1). However, in a real system, there are often other effects that increase the scattering and may also put a lower limit on the scattering probability during the transfer. Fig. 7.1 shows a generic model for a real Raman transition demonstrating some of these effects. Additionally, other practical limitations in the system like stability of the laser power and frequency also need to be taken into account.

In the experiment, we find the parameter range that gives the best transfer efficiency using numerical simulation (see section 7.4). Nevertheless, in order to develop a general approach that can be applied to other systems, it is also important to understand the various physical mechanisms that lead to the optimal parameters. Therefore, in this section, we will discuss some of the most important effects on the transfer efficiency at qualitative and semiquantitative level. Due to experimental



Figure 7.1: Generic model for a real Raman transition. The initial state $|i\rangle$ and the final state $|f\rangle$ has a energy difference δ and are coupled by two Raman beams with frequencies and single photon Rabi frequencies of ν_1, Ω_1 and ν_2, Ω_2 respectively. The corresponding matrix elements (arbitrary unit) are M_1 and M_2 . The Raman beams are detuned by Δ from the primary excited state $|e\rangle$, which has a decay rate of Γ_e . We also consider additional states near the initial ($|i'\rangle$), final ($|f'\rangle$) and intermediate excited $|e'\rangle$ states which are separated from the corresponding Raman transition states by ω'_i, ω'_f and ω'_e respectively. Only one additional state of each kinds are included to simplify the discussion without loss of generality.

constraint, we will assume that the single photon detuning is much smaller than the frequency of each individual beams, i.e. $\Delta \ll \nu_1, \nu_2$.

7.2.1 ADDITIONAL INITIAL AND FINAL STATES

First, we will discuss the effect of $|i'\rangle$ and $|f'\rangle$ states near the initial and final states. These states can be coupled to the excited state $|e\rangle$ by the Raman beams, which can in turn be coupled to the initial

and final states by an off-resonance Raman transition. The leakage is suppressed by the detuning from the Raman resonance, i.e. ω'_i and ω'_f . This puts a limit on the Raman Rabi frequency Ω_R to be smaller than the smallest energy gap, which in turns puts a limit on the minimum Raman transfer time. In our experiment, the minimum energy gap comes from axial motional excitation of the atomic initial states which is between $2\pi \times 10 - 30$ kHz depending on the trap depth used. The typical Raman π time we can realize is $0.5 - 5$ ms so this effect is not a major limiting factor for our transfer efficiency.

7.2.2 ADDITIONAL EXCITED STATES

Next, we will consider the effect of the $|e'\rangle$ state near the excited intermediate state. These states can be coupled to the ground states, both $|i\rangle$ and $|f\rangle$, by the Raman beams and can cause a change in both the Raman Rabi frequency and the scattering rate. The total Raman Rabi frequency (Fig. 7.2A) is,

$$\Omega_{Raman} = \frac{\Omega_1 \Omega_2}{2\Delta} + \frac{\Omega'_1 \Omega'_2}{2(\Delta - \omega'_e)}$$

where Ω'_1 and Ω'_2 are the single photon Rabi frequencies coupling $|e'\rangle$ to $|i\rangle$ and $|f\rangle$ respectively.

Depending on whether $\Omega'_1 \Omega'_2$ has the same (orange line) or different (blue line) sign as $\Omega_1 \Omega_2$, the total Raman Rabi frequency may be cancelled or enhanced between the two excited states. On the other hand, the total scattering rate (Fig. 7.2B) is almost always increased due to the additional state, creating a local minimum between the excited states. Combining the two effects, the ratio between the Raman Rabi frequency and the scattering rate, which determines the transfer efficiency, always

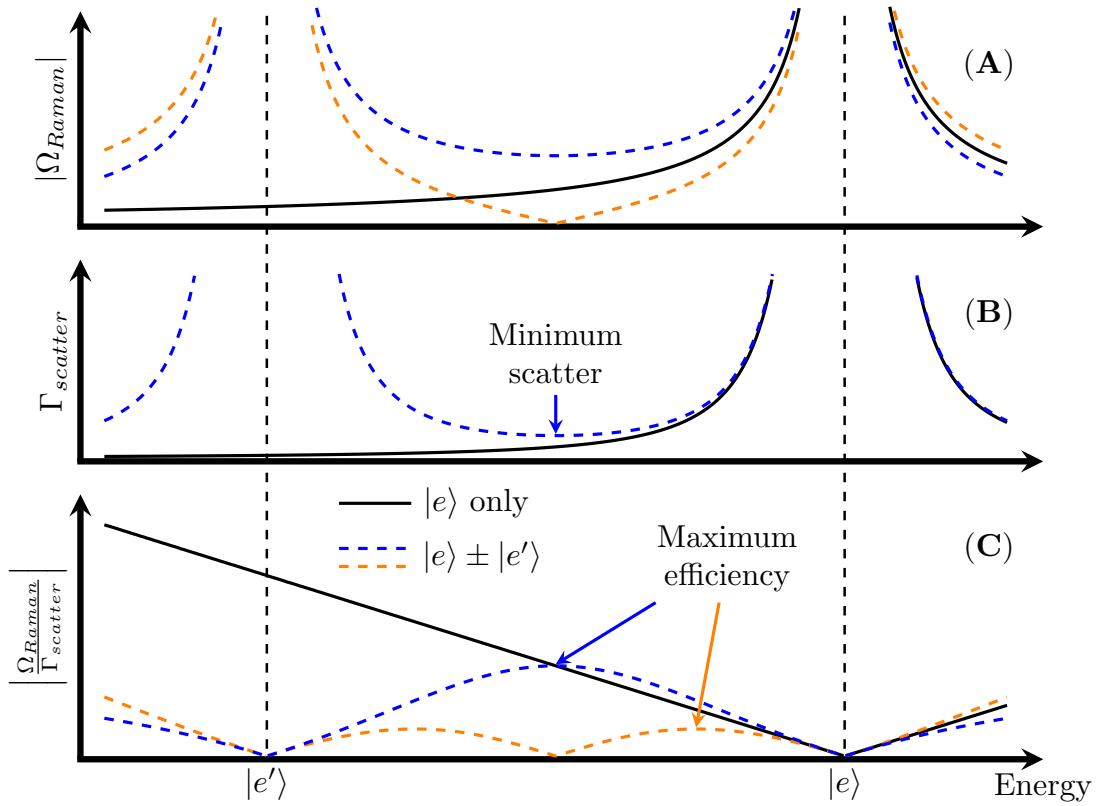


Figure 7.2: Effect of additional excited states $|e'\rangle$ on the Raman transition efficiency. (A) Depending on the sign of the coupling, there could be constructive (blue) or destructive (orange) interference on the Raman Rabi frequency Ω_{Raman} . (B) Increased scattering rate $\Gamma_{scatter}$ caused by $|e'\rangle$ with a minimal between the two states. (C) Optimal detunine exists between the two states with maximum transfer efficiency corresponds to a fraction of the state spacing.

have local maximum between the excited states (Fig. 7.2C).

Despite the difference in the position and value of the maximum for different $|e'\rangle$ parameters, we can summarize the effect on the transfer efficiency as a limit on the maximum detuning Δ_{max} to a fraction of the spacing between the excited states (ω'_e). As an example, the blue and orange maxima in Fig. 7.2C corresponds to a limit on single photon detuning of $0.5\omega'_e$ and $0.15\omega'_e$. As one would expected, a larger excited state spacing usually result in a larger detuning limit and a better transfer efficiency.

Summarizing the effect of additional excited state as a single number Δ_{max} allows us to keep using the equation for Raman transition with minor corrections and makes it easier to compare different state selection and transition schemes. It is also worth noting that although only one additional excited state $|e'\rangle$ is considered here, this result can be generalized when more excited states are taken into account as well. These states introduces additional smooth variation in both the Raman Rabi frequency and scattering rate and the effects on the final transition efficiency can be similarly treated as a change in the maximum detuning.

7.2.3 CROSS COUPLING BETWEEN LIGHT ADDRESSING INITIAL AND FINAL STATES

Due to the small energy separation between the initial and final state δ , the cross coupling of the laser addressing the initial/final state on the final/initial state is another important effect in our experiment. Without the cross coupling, the total off resonance scattering rate for the initial and the final states is

$$\Gamma_{scatter0} = \frac{\Gamma_e (\Omega_1^2 + \Omega_2^2)}{4\Delta^2}$$

For a given Raman Rabi frequency $\Omega_{Raman} \propto \Omega_1 \Omega_2$, this is minimized when $\Omega_1 = \Omega_2$.

When cross coupling is taken into account, however, the total scattering rate becomes, *

$$\Gamma_{scatter} = \frac{\Gamma_e \Omega_1^2}{4M_1^2} \left(\frac{M_1^2}{\Delta^2} + \frac{M_2^2}{(\Delta + \delta)^2} \right) + \frac{\Gamma_e \Omega_2^2}{4M_2^2} \left(\frac{M_2^2}{\Delta^2} + \frac{M_1^2}{(\Delta - \delta)^2} \right) \quad (7.1)$$

$$\propto \frac{\Gamma_e P_1}{4} \left(\frac{M_1^2}{\Delta^2} + \frac{M_2^2}{(\Delta + \delta)^2} \right) + \frac{\Gamma_e P_2}{4} \left(\frac{M_2^2}{\Delta^2} + \frac{M_1^2}{(\Delta - \delta)^2} \right) \quad (7.2)$$

where $P_{1,2} \propto \Omega_{1,2}^2/M_{1,2}^2$ are the powers of the laser beams 1 and 2. When $\delta \ll \Delta$ such as our experiment,

$$\begin{aligned} \Gamma_{scatter} &\approx \frac{\Gamma_e (M_1^2 + M_2^2)}{4\Delta^2} \left(\frac{\Omega_1^2}{M_1^2} + \frac{\Omega_2^2}{M_2^2} \right) \\ &\propto \frac{\Gamma_e (M_1^2 + M_2^2)}{4\Delta^2} (P_1 + P_2) \end{aligned}$$

For a given Raman Rabi frequency $\Omega_{Raman} \propto \Omega_1 \Omega_2 \propto \sqrt{P_1 P_2}$, this is minimized when $P_1 = P_2$. Hence, due to the strong cross coupling, we need to use the same power in both Raman beams rather than adjusting the powers to match their single photon Rabi frequencies.

Moreover, at the minimum scattering rate, we have $\Omega_2 = \Omega_1 M_2/M_1$ and the ratio between

*Here we assume that the matrix elements are the same for the two beams. This is the case when the two beams have the same polarization as in our experiment. This effect can be minimized or eliminated by selecting different polarizations for the two laser frequencies that does not couple to the other initial/final state. This would also require choosing an excited state with the same or lower angular momentum as the ground states in order to avoid cross coupling to different excited states.

Raman Rabi frequency and scattering rate is,

$$\begin{aligned}
\frac{\Omega_{Raman}}{\Gamma_{scatter}} &= \frac{\Omega_1 \Omega_2}{2\Delta} \frac{4\Delta^2}{\Gamma_e (M_1^2 + M_2^2)} \bigg/ \left(\frac{\Omega_1^2}{M_1^2} + \frac{\Omega_2^2}{M_2^2} \right) \\
&= \frac{2\Delta \Omega_1 \Omega_2}{\Gamma_e (M_1^2 + M_2^2)} \bigg/ \left(\frac{\Omega_1^2}{M_1^2} + \frac{\Omega_2^2}{M_2^2} \right) \\
&= \frac{\Delta \Omega_1^2 M_2}{\Gamma_e M_1 (M_1^2 + M_2^2)} \frac{M_1^2}{\Omega_1^2} \\
&= \frac{\Delta}{\Gamma_e} \frac{M_1 M_2}{M_1^2 + M_2^2}
\end{aligned}$$

Therefore, for a given excited state linewidth Γ_e and maximum detuning (section 7.2.2) the transfer efficiency maximizes for the smallest $M_1 M_2 / (M_1^2 + M_2^2)$ which happens when the ratio M_1 / M_2 is the closest to 1.

The light shift of the Raman resonance is similarly affected by the cross coupling. The differential light shift between the initial and the final state determines the resonance fluctuation as a function of light intensity fluctuation. The ration between the light shift and the Raman Rabi frequency, i.e. line width, determines the stability requirement of our laser indensity. With cross coupling, the differential shift is (assuming $\delta \ll \Delta$),

$$\begin{aligned}
\Delta \delta &\approx \frac{\Omega_1^2}{4\Delta} - \frac{\Omega_1^2 M_2^2}{4\Delta M_1^2} - \frac{\Omega_2^2}{4\Delta} + \frac{\Omega_2^2 M_1^2}{4\Delta M_2^2} \\
&= \frac{M_1^2 - M_2^2}{4\Delta} \left(\frac{\Omega_1^2}{M_1^2} + \frac{\Omega_2^2}{M_2^2} \right) \\
&\propto \frac{M_1^2 - M_2^2}{4\Delta} (P_1 + P_2)
\end{aligned}$$

which is also minimized when $P_1 = P_2$ at a given Raman Rabi frequency.

The ratio with the Raman Rabi frequency is,

$$\begin{aligned}\frac{\Delta\delta}{\Omega_{Raman}} &\approx \frac{M_1^2 - M_2^2}{4\Delta} \left(\frac{\Omega_1^2}{M_1^2} + \frac{\Omega_2^2}{M_2^2} \right) \frac{2\Delta}{\Omega_1\Omega_2} \\ &= \frac{M_1^2 - M_2^2}{2\Omega_1\Omega_2} \left(\frac{\Omega_1^2}{M_1^2} + \frac{\Omega_2^2}{M_2^2} \right) \\ &= \frac{M_1^2 - M_2^2}{M_1M_2}\end{aligned}$$

the absolute value of which is also minimized when the ratio M_1/M_2 is the closest to 1.

Due to the coupling strength difference, we have $M_2 \gg M_1$ in our experiment, which means,

$$\left| \frac{\Delta\delta}{\Omega_{Raman}} \right| \approx \frac{M_2}{M_1}$$

In order to keep the resonance stable within the linewidth of the Raman resonance, i.e. Ω_{Raman} , we need to maintain a relative stability of $\Delta\delta$, therefore relative stability of the laser power to better than M_1/M_2 .

7.3 RAMAN TRANSFER VERSUS STIRAP

An alternative method often used to create and prepare the internal states of ultracold molecule is stimulated Raman adiabatic passage (STIRAP). Compared to Raman transition, which uses detuning from the excited state to reduce scattering during the transfer, STIRAP relies on a superposition between the initial and final state as a dark state to achieve the same goal. The dark state in STIRAP

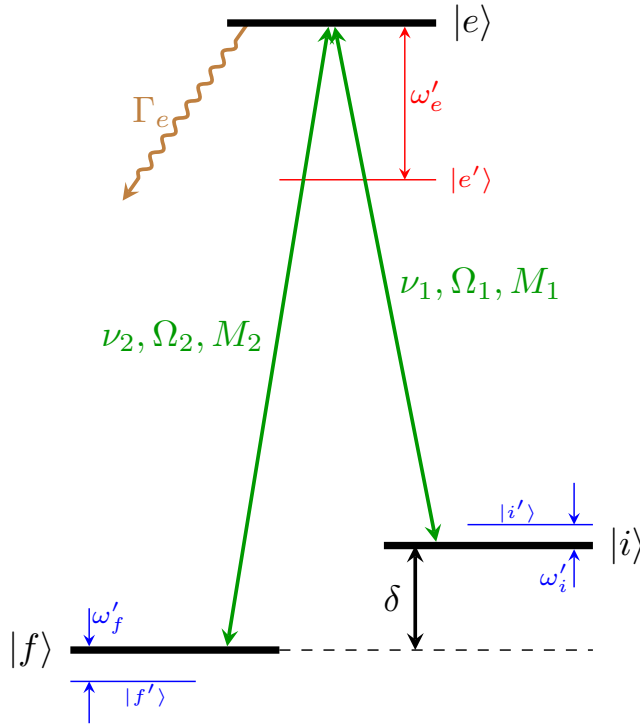


Figure 7.3: Generic model for a real STIRAP similar to Fig. 7.1. Differences are that the two beams are now on resonant with $|e\rangle$ and the Ω_1 and Ω_2 now represent the maximum single photon Rabi frequency during the STIRAP pulse.

is created due to a destructive interference of transition from the initial and final state to the excited state.

Similar to Raman transfer, STIRAP in an ideal three-level system can achieve full coherent transfer with arbitrarily small scattering probability when given unlimited time and power budget. However, in reality, states and coupling that exist outside the ideal three-level system always cause a non-zero probability of scattering loss (see Fig. 7.3). In this section, we will apply the approach we took for Raman transition to STIRAP. We will then compare the loss caused by different practical limitations and discuss which approach should be taken under certain circumstance.

7.3.1 ADDITIONAL INITIAL AND FINAL STATES

Similar to Raman transition (section 7.2.1), the additional initial and final states causes potential leakage out of the three-level system. This limits the minimum time of the transfer in a way similar to that of Raman transition.

7.3.2 ADDITIONAL EXCITED STATES

7.3.3 CROSS COUPLING BETWEEN LIGHT ADDRESSING INITIAL AND FINAL STATES

7.3.4 CONCLUSION

7.4 STATES SELECTION

(Differential Light Shift) (Scattering)

7.4.1 EXCITED STATE SELECTION

7.4.2 GROUND STATES SELECTION

FINAL MOLECULAR STATE

INITIAL ATOMIC STATE

7.5 RAMAN TRANSFER RESULTS

7.5.1 SCALING OF RAMAN TRANSITION PARAMETERS

8

Conclusion



Computer Control Hardware Specification

NIDAQ

FPGA

DDS

USRP



Full Raman Sideband Cooling Sequence

Each Raman pulse in the cooling sequence is followed immediately by an optical pumping pulse.

The full parameters for the Raman pulses, including the cooling “axis”, the sideband “order (Δn)”, the cooling frequency “ δ' ”, the carrier ($\Delta n = 0$) frequency “ δ'_0 ”, the pulse “duration”, the pulse strength in “ Ω_0 ”, and the beam of which a non-uniform “power ramp” is applied, are listed in 6 groups below. The applied cooling frequency, δ' , is the two-photon detuning given relative to the

zero-field $F = 1$ and $F = 2$ hyperfine splitting of $1.7716261288(10)$ GHz^{Steck}. Due to the Stark shifts of the Raman beams, the carrier transition, δ'_0 , varies with the power of the Raman beams. δ'_0 is given also relative to the zero-field hyperfine splitting. The strength of the pulses given in Ω_0 determines the two-photon Rabi frequency, $\Omega_{n,\Delta n} = \Omega_0 \langle n | e^{i\vec{k}\cdot\vec{r}} | n + \Delta n \rangle$. We adopt the convention that a π -pulse between state n and $n + \Delta n$ requires a duration $\pi/\Omega_{n,\Delta n}$. The difference between δ' and δ'_0 gives the motional sideband frequency, δ . Many Raman pulses include a “power ramp” with a Blackman envelope^{Kasevich & Chu} to minimize off-resonant excitations. Because each Raman pulse is a product of two spatial- and temporal-overlapped laser beams, the “power ramp” is applied only to the beam that has the smaller light shift (we label the beam by the corresponding F number) while the other beam has a square-pulse shape. For a Raman pulse with a power ramp, the Rabi frequency gives the arithmetic mean over the duration of the pulse.

GROUP 1

This group is repeated 4 times.

Axis	Δn	δ' (MHz)	δ'_0 (MHz)	Duration (μs)	Ω_0 (kHz)	Power ramp
x	-2	19.625	18.649	44.1	$2\pi \times 23$	F ₁
y	-2	19.615	18.648	28.6	$2\pi \times 35$	F ₁
x	-1	19.130	18.649	36.9	$2\pi \times 23$	F ₁
y	-1	19.615	18.648	24.0	$2\pi \times 35$	F ₁

GROUP 2

This group is repeated 5 times.

Axis	Δn	δ' (MHz)	δ'_0 (MHz)	Duration (μs)	Ω_0 (kHz)	Power ramp
z	-5	19.030	18.605	81.5	$2\pi \times 16$	F ₂
x	-2	19.625	18.649	44.1	$2\pi \times 23$	F ₁
z	-4	18.940	18.605	76.3	$2\pi \times 16$	F ₂
y	-2	19.615	18.648	28.6	$2\pi \times 35$	F ₁
z	-5	19.030	18.605	81.5	$2\pi \times 16$	F ₂
x	-1	19.130	18.649	36.9	$2\pi \times 23$	F ₁
z	-4	18.940	18.605	76.3	$2\pi \times 16$	F ₂
y	-1	19.130	18.648	24.0	$2\pi \times 35$	F ₁

GROUP 3

This group is repeated 6 times.

Axis	Δn	δ' (MHz)	δ'_0 (MHz)	Duration (μs)	Ω_0 (kHz)	Power ramp
z	-4	18.940	18.605	76.3	$2\pi \times 16$	F ₂
x	-2	19.625	18.649	44.1	$2\pi \times 23$	F ₁
z	-3	18.858	18.605	70.2	$2\pi \times 16$	F ₂
y	-2	19.615	18.648	28.6	$2\pi \times 35$	F ₁
z	-4	18.940	18.605	76.3	$2\pi \times 16$	F ₂
x	-1	19.130	18.649	36.9	$2\pi \times 23$	F ₁
z	-3	18.858	18.605	70.2	$2\pi \times 16$	F ₂
y	-1	19.130	18.648	24.0	$2\pi \times 35$	F ₁

GROUP 4

This group is repeated 7 times.

Axis	Δn	δ' (MHz)	δ'_0 (MHz)	Duration (μ s)	Ω_0 (kHz)	Power ramp
z	-3	18.858	18.605	70.2	$2\pi \times 16$	F ₂
x	-2	19.625	18.649	44.1	$2\pi \times 23$	F ₁
z	-2	18.773	18.605	62.7	$2\pi \times 16$	F ₂
y	-2	19.615	18.648	28.6	$2\pi \times 35$	F ₁
z	-3	18.858	18.605	70.2	$2\pi \times 16$	F ₂
x	-1	19.130	18.649	36.9	$2\pi \times 23$	F ₁
z	-2	18.773	18.605	62.7	$2\pi \times 16$	F ₂
y	-1	19.130	18.648	24.0	$2\pi \times 35$	F ₁

GROUP 5

This group is repeated 10 times.

Axis	Δn	δ' (MHz)	δ'_0 (MHz)	Duration (μs)	Ω_0 (kHz)	Power ramp
z	-2	18.773	18.605	62.7	$2\pi \times 16$	F ₂
x	-1	19.130	18.649	36.9	$2\pi \times 23$	F ₁
z	-1	18.685	18.605	52.5	$2\pi \times 16$	F ₂
y	-1	19.130	18.648	24.0	$2\pi \times 35$	F ₁
z	-2	18.773	18.605	62.7	$2\pi \times 16$	F ₂
x	-1	19.130	18.649	70.0	$2\pi \times 23$	F ₁
z	-1	18.685	18.605	52.5	$2\pi \times 16$	F ₂
y	-1	19.130	18.648	46.0	$2\pi \times 35$	F ₁

GROUP 6

This group is repeated 30 times.

Axis	Δn	δ' (MHz)	δ'_0 (MHz)	Duration (μs)	Ω_0 (kHz)	Power ramp
z	-1	18.683	18.605	78.7	$2\pi \times 11$	F ₂
z	-1	18.683	18.605	135.0	$2\pi \times 11$	F ₂
z	-1	18.685	18.605	78.7	$2\pi \times 11$	F ₂
x	-1	19.130	18.649	36.9	$2\pi \times 23$	F ₁
y	-1	19.130	18.648	24.0	$2\pi \times 35$	F ₁
z	-1	18.685	18.605	78.7	$2\pi \times 11$	F ₂
z	-1	18.685	18.605	135.0	$2\pi \times 11$	F ₂
z	-1	18.685	18.605	78.7	$2\pi \times 11$	F ₂
x	-1	19.130	18.649	70.0	$2\pi \times 23$	F ₁
y	-1	19.130	18.648	46.0	$2\pi \times 35$	F ₁

References

- [Hutzler et al.] Hutzler, N. R., Liu, L. R., Yu, Y., & Ni, K.-K. Eliminating light shifts for single atom trapping. 19(2), 023007.
- [Kasevich & Chu] Kasevich, M. & Chu, S. Laser cooling below a photon recoil with three-level atoms. 69(12), 1741–1744.
- [Kaufman et al.] Kaufman, A. M., Lester, B. J., & Regal, C. A. Cooling a Single Atom in an Optical Tweezer to Its Quantum Ground State. 2(4), 041014.
- [Meekhof et al.] Meekhof, D. M., Monroe, C., King, B. E., Itano, W. M., & Wineland, D. J. Generation of Nonclassical Motional States of a Trapped Atom. 76(11), 1796–1799.
- [Steck] Steck, D. A. Sodium D Line Data.
- [Thompson et al.] Thompson, J. D., Tiecke, T. G., Zibrov, A. S., Vuletić, V., & Lukin, M. D. Coherence and Raman Sideband Cooling of a Single Atom in an Optical Tweezer. 110(13), 133001.